International Journal of Heat and Fluid Flow 31 (2010) 19–31

Contents lists available at ScienceDirect

International Journal of Heat and Fluid Flow

journal homepage: www.elsevier.com/locate/ijhff

Heat transfer and pressure drop in two-pass rib-roughened square channels with bleed from sharp bend

Shyy Woei Chang [a,*], Zong-Xian Cai [b,1]

[a] Thermal Fluids Laboratory, National Kaohsiung Marine University, No. 142, Haijhuan Road, Nanzih District, Kaohsiung City 81143, Taiwan, ROC
[b] Department of Marine Engineering, National Kaohsiung Marine University, No. 142, Haijhuan Road, Nanzih District, Kaohsiung City 81143, Taiwan, ROC

ARTICLE INFO

Article history:
Received 19 January 2009
Received in revised form 29 October 2009
Accepted 3 November 2009
Available online 22 December 2009

Keywords:
Two-pass rib-roughened bleed channel
Gas turbine blade cooling

ABSTRACT

This experimental study investigates the heat transfer, pressure drop and thermal performance factor for the two-pass rib-roughened channel with and without bleed from its sharp bend. Detailed distributions of Nusselt number (Nu) and dimensionless wall temperature (η_w) over the rib floor with coolant extractions from three different locations on the outer wall of the sharp bend at 0%, 10%, 20%, 30% of the total airflow rate are comparatively analyzed with $5000 < Re < 25{,}000$. Area-averaged Nu and pressure drop coefficients (f) for the entire two-pass ribbed channel with and without bleed are generated with thermal performance factors (η) compared. The bleed from the outer wall of the sharp bend provides considerable heat transfer enhancements (HTE) over the turning section with substantial reductions in pressure drops; while undermines both Nu and η_w performances in the outlet-leg from the no-bleed conditions. Thermal performance factors for the bleed channel at each Re and bleed condition tested are improved from the no-bleed references. Empirical Nu and f correlations are derived for the present two-pass rib-roughened square channel with and without bleed.

1. Introduction

Modern gas turbine blades are protected by the cooling system to prevent thermal damages under the working environments at temperatures about 1800–2000 K. Current cooling schemes for gas turbine blades generally combine internal and film cooling. Airflows fed from the compressor are channeled into the serpentine passages within these blades and partially ejected into the hot gas stream through the film-cooling holes. Although the coolant flow is essential for assuring the life and safety standard of a gas turbine blade, the consumption of high pressure air from the compressor is a penalty on the engine thermal efficiency. The minimization of coolant flow while improving the engine performance is a design goal for engine developments. To fulfill such cutting edge design goals, the individual and interdependent flow and heat transfer phenomena for both the internal and film coolant flows need to be understood. In this respect, the pressure gradients induced around these film-cooling holes, which are dependent on the geometries of the internal coolant channel, not only affect the bleeds and therefore the coolant-film attached on the external blade surface but also modify the structures of internal coolant flow from the no-bleed conditions. The interactions between the internal coolant flow and the external coolant-film are thus considerably affected by the locations, geometries and arrangements of the film-cooling holes (Grag, 2002). Influences of bleeds on the performances of heat transfer and pressure drop for simulated coolant passages inside turbine blades are accordingly investigated (Taslim et al., 1995; Shen et al., 1996; Ekkad et al., 1998; Thurman and Poinsatte, 2001; Chanteloup and Bölics, 2002; Chang et al., 2007, 2008). In general, the allocations of bleeds depend on the distributions of heat flux over the external blade surface. As indicated in Fig. 1, airflows are often bled from the ribbed floors of the internal coolant channels over the pressure and suction surfaces of these blades. At the trailing edge of the turbine blade, bleeds are arranged along the apical sidewall of the trapezoidal internal coolant passage. For cooling and anti-fouling purposes, coolant is also ejected from the sharp bend of the serpentine internal channels via the bleed holes through the tip of the blade toward the shroud. As these bleeds break boundary layers and modify the local pressure gradients, the distributions of mass flux and hence the flow structures of internal coolant flows, the cooling performances over all the constituent channel walls are affected by the bleeds. Previous investigations in this respect have not been performed to a large extent and only focused on the heat transfer performances with bleeds from the straight passages. Taslim et al. experimentally examined the effects of bleeds on heat transfer in the trapezoidal straight passage roughened by transverse ribs (Taslim et

* Corresponding author. Tel.: +886 7 8100888x5216.
E-mail addresses: swchang@mail.nkmu.edu.tw (S.W. Chang), kuei@mail.nkmu.edu.tw (Z.-X. Cai).
[1] Tel.: +886 919616266.

0142-727X/$ - see front matter © 2009 Published by Elsevier Inc.
doi:10.1016/j.ijheatfluidflow.2009.11.001

Nomenclature

English symbols

A, B, L, M, N	correlation coefficients
C_p	constant-pressure specific heat of the coolant (J kg^{-1} K^{-1})
d	hydraulic diameter of test channel (m)
e	rib land (m)
f	pressure drop coefficient = $\Delta P/(0.5\rho V_{in}^2)$ $(d/4T_L)$
f_∞	friction factor evaluated from Blasius equation = $0.079Re^{-0.25}$
H	rib height (m)
k_f	thermal conductivity of coolant (Wm^{-1} K^{-1})
L	length of test channel (m)
L_T	channel width of sharp bend (m)
$\dot{m}$	total coolant mass flow rate into test channel (kg s^{-1})
Nu	local Nusselt number over two-pass rib floor = $qd/k_f(T_w - T_b)$
Nu_∞	Dittus–Boelter Nusselt number correlation = $0.023Re^{0.8}Pr^{0.4}$
$\overline{Nu}$	area-averaged Nusselt number
P	rib pitch (m)
ΔP	pressure drop over entire test channel (N m^{-2})
Q_f	total convective heating power (W)
q	convective heat flux (W m^{-2})
Re	Reynolds number based on channel hydraulic diameter = $\rho V_{in} d/\mu$
T_b	fluid bulk temperature (K)
ΔT_f	reference fluid temperature difference = $Q_f/(\dot{m} \times C_p)$
T_L	total length of two-pass test channel (m)
T_w	local wall temperature at two-pass rib floor (K)
V_{in}	mean flow velocity at the entrance of inlet-leg (m s^{-1})
W	spanwise width of turning section (m)
W_H	channel height (m)
$W_{I,O}$	channel width of inlet (outlet) leg (m)
x, y	coordinates in streamwise and spanwise directions (m)

Subscripts

I	inlet-leg
T	turning section
O	outlet-leg

Greek symbols

α	rib attack angle (deg)
η	thermal performance factor = $[Nu/Nu_\infty]/[(f/f_\infty)^{1/3}]$
η_w	dimensionless wall temperature = $T_w/\Delta T_f$
$\overline{\eta_w}$	area averaged dimensionless wall temperature
μ	dynamic viscosity of fluid (kg s^{-1} m^{-1})
ρ	density of test fluid (kg m^{-3})

al., 1995). Shen et al. performed detailed heat transfer and shear stress measurements in a convergent duct roughened by transverse ribs with bleeds (Shen et al., 1996). These bleeds from the rib floor alter the flow structures between two adjoining transverse ribs in the manner of reducing the extent of flow separation behind each rib. Reductions of flow re-circulating regions behind the ribs along with the local heat transfer enhancements in the vicinity of bleed holes by breaking boundary layers could elevate the spatially averaged heat transfer by about 25%. Ekkad et al. examined the heat transfer performances of a turbulated two-pass square channel with the bleeds along the centerline of the rib floor at the midways between two successive ribs (Ekkad et al., 1998). The distinct difference in *Nu* distributions along the rib floor with and without bleeds is characterized by the minor heat transfer peak immediate downstream of each bleed hole. Regional averaged heat transfer levels for the bleed ribbed channel with 20–25% of coolant extractions are similar to the likewise channel without bleed (Ekkad et al., 1998). Thurman and Poinsatte examined the detailed heat transfer distributions in a triple-pass channel roughened by transverse ribs with bleeds in the first passage (Thurman and Poinsatte, 2001). Three different bleed conditions, namely the uniform, increasing and decreasing bleeds per each bleeding hole, were tested. Among this comparative group examined by Thurman and Poinsatte, the uniform bleed provided the higher heat transfer enhancements (Thurman and Poinsatte, 2001). At the higher Reynolds numbers (*Re*) for the cases with bleeds, heat transfer enhancements due to the increased mixing and boundary layer removal are less pronounced. By allocating the bleeds with the so-called rib-between-holes and ribs-near-holes configurations, the backward-**C**-shaped and **C**-shaped *Nu* patterns were respectively developed on the rib floors. Chanteloup and Bölics carried out the detailed PIV measurements for the flows in a two-pass channel roughened by 45° ribs with bleeds in the second passage (Chanteloup and Bölics, 2002). As the coolant was only extracted from *one side* of the ribbed channel, the streamwise symmetrical velocity profile in the likewise no-bleed channel was distorted toward the bleed wall that generated a strongly asymmetrical secondary flow motion. As a result, the pair of rib-tripped baseline secondary flows in the channel without bleed was considerably modified by such one-wall bleeds. In the channel with one-wall bleeds, the baseline secondary flow cells developed in the no-bleed channel had almost disappeared along the bleed wall; while its counter-rotating secondary flow cell opposite to the bleed wall was enlarged. As the bleeds from one ribbed wall considerably affected the rib induced secondary flows through the entire channel (Chanteloup and Bölics, 2002), the heat transfer distributions on all constituent walls with and without bleeds were modified from the

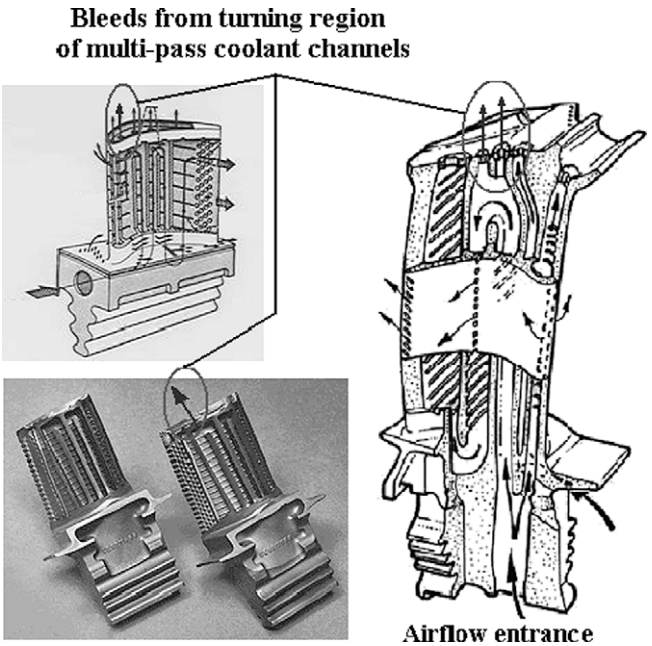

Fig. 1. Internal coolant channels of gas turbine blades with bleeds.

no-bleed conditions. By way of varying the channel aspect ratio and/or the bleeding wall where coolant extractions takes place therefore affect the impacts of bleeds on the heat-transfer and pressure-drop performances over the entire ribbed channel (Chang et al., 2007). With bleeds from the rib-roughened wall, the extractions of coolant bleed off the boundary layers over the rib floor and reduce the extent of the flow recirculation behind each rib, which influences in combination can elevate the regional Nusselt numbers (*Nu*) surrounding the bleeding holes. But these favorable flow mechanisms for regional *Nu* elevations around the bleeding holes are absent in the rib-roughened channels with bleeds from the sidewall. Instead, such sidewall extractions weaken the strengths of both the rib-tripped secondary flows and the downstream flow momentums, which together elevate the wall temperatures over the rib floor by decreasing local *Nu* and reducing the airflow rate that raises the fluid temperatures (Chang et al., 2007, 2008). It is clear that the locations of bleeds from a rib-roughened channel have profound influences on the heat-transfer and pressure-drop performances in the ribbed channels (Chang et al., 2007). Thus the impacts of coolant extraction from the sharp bend of a multi-pass ribbed channel on local and regionally averaged heat transfer performances as well as on the pressure drop characteristics need to be examined.

For multi-pass ribbed channels (Grag, 2002; Thurman and Poinsatte, 2001; Chanteloup and Bölics, 2002; Ekkad and Han, 1997; Ekkad et al., 2000; Chanteloup and Wolfersdorf, 2004; Viswanathan and Tafti, 2006), the heat transfer performances in the straight ribbed legs away from the sharp bend are typical for the periodic flow behaviors with repetitive streamwise *Nu* variations along the rib floor. The secondary flows tripped by ribs dominate the heat transfer performances in the straight leg until the flow has entered the sharp bend. As the coolant flow approaches the sharp bend, it accelerates locally and separates at the sharp edge of the bend. Viswanathan and Tafti reported that such bend-induced separated region occupied the central 25–40% of the duct height (Viswanathan and Tafti, 2006). Additional re-circulating cells developed in the outer corners of the bend and at the downstream bend on the inner wall of the outlet ribbed leg. Locations with high *Nu* in the bending region emerge at the downstream outer wall of the bend due to the impingement of bulk stream through the bend. At the center of the 180° bend, the Dean-vortices that impinge on the inner and outer walls in the bend become the dominant flow features to induce high heat transfer rates at these walls (Viswanathan and Tafti, 2006). Due to the flow features induced by the 180° sharp bend, the *Nu* distributions in the bend region are different from those in the inlet and outlet ribbed legs. In the sharp bend, no high heat transfer gradients occurred and the decreases of *Nu* up to 20% in the bend from the averaged *Nu* in the inlet ribbed leg were experimentally observed (Chanteloup and Wolfersdorf, 2004). The recovery of repetitive *Nu* patterns in the ribbed outlet-leg was generally initiated from the first rib location downstream of the bend and re-developed again after about 5 hydraulic diameters downstream from the bend (Ekkad and Han, 1997; Ekkad et al., 2000; Chanteloup and Wolfersdorf, 2004; Viswanathan and Tafti, 2006). The coolant extractions from the outer wall of the 180° sharp bend, as typified in Fig. 1 as the bleeds from the blade tip toward the shroud, can certainly alter the complex flow structures developed in the bend. But most of previous investigations studied the thermal fluid performances for the multi-pass channels with bleeds from the static straight passages, regardless of the wide cooling applications which bleed coolant from the sharp bend of a multi-pass coolant channel for both static and rotor blades. With rotor blade cooling applications, the orthogonal rotation, as shown by many researchers (Iacovides et al., 2001; Iacovides and Launder, 2007; Johnson et al., 1994; Parsons et al., 1995), will further modify the flow and thermal developments from the static multi-pass ribbed channels. As a primary attempt to reveal the impact of bleed from the sharp bend on the thermal performance of the twin-pass ribbed channel, this study investigates the heat transfer and pressure drop in the static two-pass rib-roughened channels with the bleed from the sharp bend. Detailed *Nu* distributions over the rib floor and the pressure drop coefficients across the two-pass channel with and without bleed are comparatively examined. Empirical correlations that evaluate the area-averaged *Nu* over the inlet-leg ($\overline{Nu}_I$), the turning region ($\overline{Nu}_T$) and the outlet-leg ($\overline{Nu}_O$) and the pressure drop coefficients across the test channel with and without bleeds are generated to assist design applications. These empirical correlations are limited for the cooling applications of static blades. Further studies involving orthogonal rotation effects are necessary for the cooling applications of gas-turbine rotor blade in which the effects of Coriolis forces and centrifugal buoyancy on flow and heat transfer need to be examined.

2. Experimental details

The test facility, the steady-state heat-loss and heat-transfer experiments as well as the method of data processing follow our previous study reported in (Chang et al., 2007). A brief description is provided as follows for the interest of completeness. The Dry and cooled airflow is guided through a set of pressure regulator and filtering unit, a mass flow meter and a needle valve where the mass flow rate of coolant is metered and adjusted. Another massflow meter after the exit of the test section measures the exit massflow rate. With the predefined coolant mass flow rate specified by the tested Reynolds number, controls of entry and vent valves obtain the targeting test conditions at the specified Reynolds number and bleed ratio. The detailed temperature distributions over the scanned rib floor are imaged by a calibrated two dimensional infrared radiometer. References to evaluate the effectiveness of heat transfer enhancement (HTE) and the pressure-drop augmentation for the present test channel are respectively evaluated from the Dittus–Boelter correlation as Nu_∞ (Dittus and Boelter, 1930), and the Blasius equation as f_∞ defined in the nomenclature. Thermal performance factors (η) are accordingly quantified as $(\overline{Nu}/Nu_\infty)/(f/f_\infty)^{1/3}$ where $\overline{Nu}$ and f are respectively the regional area-averaged *Nu* and the Fanning friction factor determined from the inlet-to-exit pressure drop of the entire test channel with and without bleed.

2.1. Test module

Fig. 2 shows the constructional details of the two-pass test module constituted by the rib-roughened inlet and outlet-legs with an 180° sharp bend. The present x–y coordinate system with origin at the entry corner of the inlet-leg is also indicated in Fig. 2. Ten pairs of square sectioned 45° ribs at a regular interval of 10 rib heights are arranged in the staggered manner on two opposite walls of each square sectioned inlet or outlet-leg. Geometric features of the two-pass channel and the rib floor are characterized by the dimensionless parameters summarized in Table 1.

The two opposite rib roughened heating surfaces (1) and (2) are made of two continuous thin stainless steel. This test section uses the 0.1 mm thick stainless steel foil to fold into the required geometrical configurations specified in Fig. 2 for the two opposite rib floors (1) and (2). Electrical current was directly passing through these two ribbed stainless steel foils (1) and (2) to generate the required Joule heat all over the rib floors and the turning region. No additional heating foil was used. The scanned two-pass ribbed heating foil (1) over which the detailed wall temperatures are detected is sandwiched between the Teflon base plate (3), the Teflon

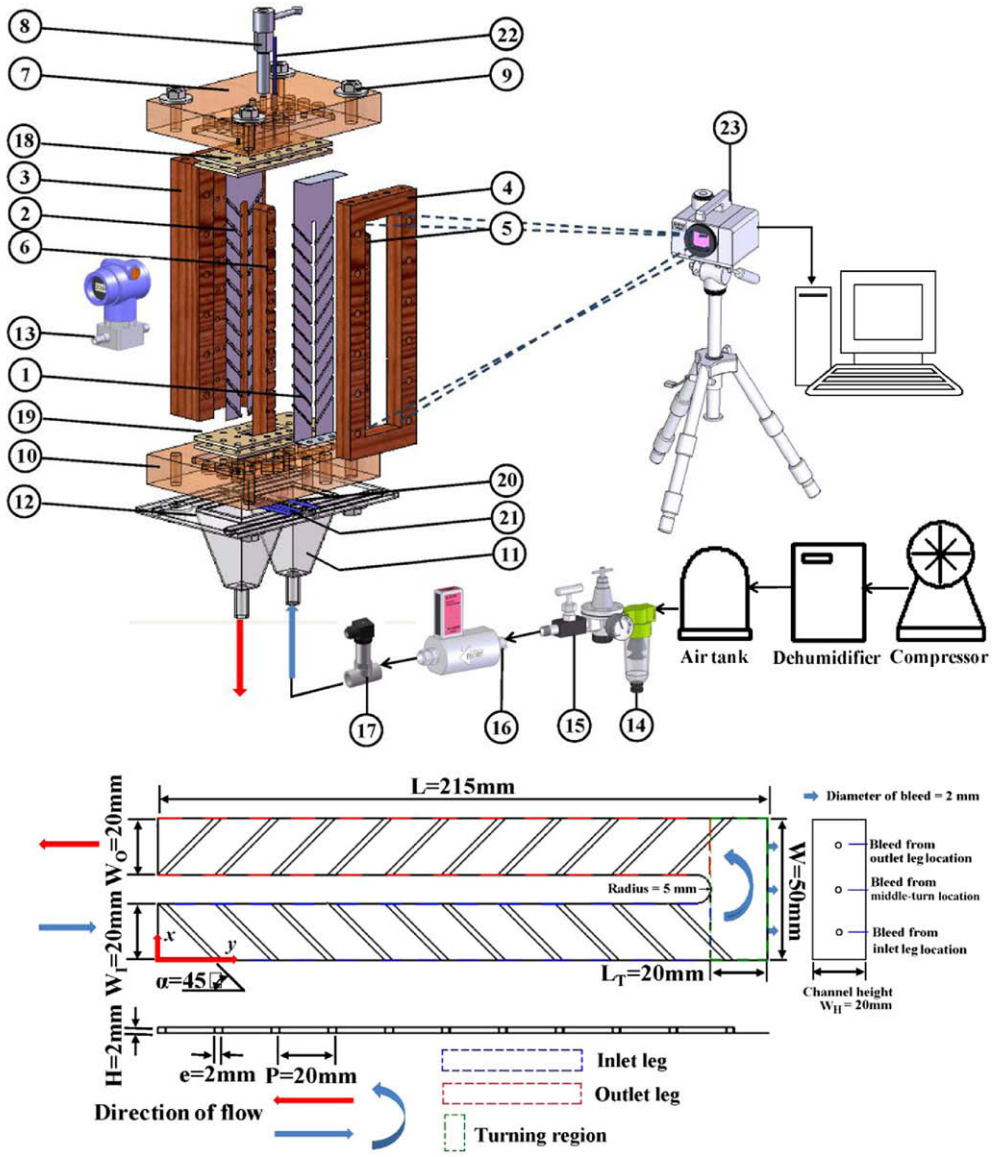

(1)(2) Ribbed heating foils
(3) Teflon base plate
(4) Teflon frame
(5) Front section of divider
(6) Central Teflon divider
(7) Outer Teflon wall
(8) Needle valve (bleed)
(9) Draw bolt
(10) Teflon bottom wall
(11) Entry plenum chamber
(12) Exit plenum chamber
(13) Micromanometer
(14) Pressure regulator and filter unit
(15) Needle valve
(16) Mass flow meter
(17) Pressure transducer
(18)(19) Copper plates
(20) Thermocouple measuring fluid entry temperature
(21) Thermocouple measuring fluid exit temperature
(22) Probing tube
(23) Infrared radiometer

Fig. 2. Constructional details of test module.

frame (4) and the front section of Teflon divider (5) to secure its position on the test channel. The Teflon base plate (3) consolidates two sidewalls and the back wall of the two-pass channel with the heating foil (2) and the central divider (6) fitted at the required locations. The Teflon central divider (6) is 195 mm long, 10 mm wide with the circular edge of radius 5 mm to form the inner wall of the sharp bend. The Teflon outer wall of the two-pass channel (7) is replaceable in order to simulate the no-bleed and three different bleed conditions. As indicated in Fig. 2, the bleed hole with diameter of 2 mm at the outer wall of the sharp bend is located at three different locations, namely at the projected centers of the inlet and outlet-legs and at the midway on the outer wall (7). A needle valve (8) is attached at the exit of the bleed hole that controls the airflow rate of the bleed. A set of mass flow meters downstream the needle valve (8) detects the airflow rate of the bleed which is controlled at 10%, 20% and 30% of the total coolant flow rate for each *Re* tested here.

The complete set of the test section is tightened by six pairs of axial bolts and four draw bolts (9) between the outer wall (2) and the bottom Teflon flange (10) which connects the divergent entry

Table 1
Geometric features of the two-pass channel and the rib floor.

Channel geometry
Channel width, $W_{I,O}$(20 mm)/channel height, W_H(20 mm) = 1 (inlet and outlet-legs)
Width of turning channel, L_T(20 mm)/channel height, W_H(20 mm) = 1 (sharp bend)
Diameter of inner circular wall of sharp bend to channel hydraulic diameter ratio (10 mm/20 mm) = 0.5
Diameter of bleed to channel height ratio (2 mm/20 mm) = 0.1
Rib floor geometry
Rib height, H(2 mm)/channel height, W_H(20 mm) = 0.1
Rib pitch, P(20 mm)/rib height, e(2 mm) = 10
Rib land, e(2 mm)/rib height, H(2 mm) = 1
Rib angle of attack (α) = 45°

(11) and the convergent exit (12) plenum chambers. The divergent entry plenum chamber (11) joins with the ribbed inlet-leg to simulate the abrupt entry condition. Through the bottom Teflon flange (10), two pressure tapings are fitted at the locations adjacent to the entry and exit planes of the two-pass channel for measuring the pressure drop over the entire test channel. These two pressure tapings are connected with the micromanometer (13) which provides the precision of 0.01 mm-H_2O with a digital display. The dry and cooled airflow from the air tank is guided through a set of pressure regulator and filtering unit (14), an entry needle valve (15), a mass flow meter (16) and a pressure transducer (17) through which the supplied total mass flow rate of coolant is metered and adjusted. Prior to entering the rib-roughened two-pass channel, the airflow enters the entry plenum chamber (11) in which the honeycomb and steel meshes are installed. The two ends of each heating foil (1) and (2) are sandwiched between two sets of copper plates (18) and (19) that connect with cables to permit the connection of electrical heating power. This heating configuration connects the electrical resistances of inlet and outlet-legs in shunt, which then joins the electrical resistance of the turning section in series. Analysis of the electrical circuit estimates the electrical resistances and the heating powers for the inlet (outlet) leg and the turning section, which consequently leads to the calculation of heat fluxes fed to these heating regions for each test condition.

The controls of entry (15) and exit (8) valves set the supplied coolant mass flow rate at the predefined value for each tested *Re* with the flow rate of the bleed remaining at the target value. The inlet fluid temperature is measured by a type K thermocouple (20) allocated at the exit of the entry plenum chamber (11). Inlet Reynolds numbers are calculated and monitored based on the total mass flow rate fed into the two-pass channel and the flow entry temperature detected by thermocouple (20). Three additional type K thermocouples (21) are equally spaced on the exit plane of the outlet-leg to measure the flow exit temperatures. The measured fluid bulk temperature (T_b) at the exit is acquired by averaging the three thermocouple measurements (21). Having completed each steady state wall temperature scan over the rib floor (1), the probing tube (22) with four equal-spaced type K thermocouples is probing into the turning region at the immediate downstream bleed location through the outer Teflon wall (7) to measure the fluid temperatures at the streamwise location corresponding to the bleed. These probing holes at the immediate downstream locations of the bleed holes along the centerline of the outer Teflon wall (7) are selectively sealed with tapings during each heat transfer test. T_b at the bleed hole is obtained by averaging these four temperature measurements collecting from the probing tube (22). Local T_b along the two-pass channel are calculated using the enthalpy balanced method based on the regional heat fluxes, the measured fluid entry temperature and the averaged fluid temperature detected by the probing tube (22). In this respect, two different airflow rates before and after the bleed location are used to determine the streamwise fluid temperature rises. At the flow exit of the outlet-leg, the comparisons of calculated and detected T_b are constantly checked. Experimental raw data are collected for subsequent data processing only if the differences between the calculated and measured T_b at the exit of the outlet-leg are less than 10%.

The detailed temperature distributions over the scanned heating foil (1) are imaged by a calibrated two dimensional infrared radiometer (23) which takes 0.3 s to complete a full field of 239×255 matrix scan. The back surface of the scanned heating foil (1) is painted black to minimize the background refection and to enhance the emission. The reference fluid temperature is selected as the local fluid bulk temperature to evaluate the local Nusselt number and all the temperature dependent fluid properties such as the thermal conductivity and viscosity of coolant. The characteristic length scale selected to define *Re* and *Nu* is the hydraulic diameter of test channel (d), which is 20 mm for the present two-pass rib-roughened channel. As there is bleeding air in the turn region, the Reynolds numbers in the inlet and outlet-legs are different. The referred *Re* for each test condition reported by this study is based on the *Re* in the inlet-leg.

2.2. Program and data processing

For steady-state heat transfer tests, the detailed wall temperature (T_w) distributions over the scanned two-pass ribbed surface with no-bleed and three bleed conditions, namely the bleed from the inlet (outlet) leg location or the middle-turn as indicated in Fig. 2, are detected at $Re = 5000$, 10,000, 15,000, 20,000, and 25,000. The steady state is assumed when the variations of wall temperatures between several successive scans at the monitoring spot over the scanned rib floor are less than 0.3 °C. To reach such steady state after either the airflow rate of the heater power is adjusted, it generally takes about 30–45 min. Having satisfied the steady state condition, the infrared thermal image program is activated to record the full-field T_w scan and transmitted to computer for subsequent data analysis. The mapping of wall temperature from the numerical temperature data file generated by the infrared thermography system is graphically performed. Having specified the dimensionless geometric ratios of the scanned area such as the channel length-to-width ratio, the complete scanned wall temperature image is screened into three regions, namely the inlet and outlet-legs and the turning section. The subsequent data reduction procedure processes these wall temperature measurements into local Nusselt numbers. Heat-transfer and pressure-drop tests are performed with a single bleed form each of the three locations through the outer wall of the bend, namely at the midway of the turning section and at the locations corresponding to the projected centerlines from the inlet and outlet-legs, with three bleed ratios (BR) of 0.1, 0.2, and 0.3 for any tested *Re*. BR is the mass flow rate ratio between the bleeding airflow rate and the total supplied airflow rate. Corresponding to each heat transfer test condition, the pressure drop across the entire two-pass ribbed channel is individually measured at the isothermal condition. With heat transfer tests, heater powers are constantly adjusted to raise the temperatures at the hottest spot on the scanned rib floor to 120 °C. Such heater power adjustments vary the fluid properties due to the variations in fluid temperatures. Airflow rates are accordingly adjusted to compensate the variations in fluid properties caused by the fluid-temperature variations in order to control the *Re* at the entry-plane of the test channel within +1% variances from the targeting values. Such *Re* control is constantly performed during each heat transfer test using the on-line monitoring program, in which the *Re* at the flow entrance is calculated based on the measured inlet fluid temperature, pressure and the massflow rate of the test coolant.

The measured raw data from heat transfer tests are converted into local Nu using the equation of $Nu = qd/k_f(T_w - T_b)$, in which the local convective heat flux (q) is calculated from the regional heat flux with the external heat loss flux subtracted. The heat loss characteristics are disclosed after a series of heat loss calibration tests. To perform the heat loss calibration tests, the flow is blocked off and the thermal insulating material is filled in the flow passage so that the heating power fed into the test section is entirely lost to the ambience through the conduction networks formulated by the test assembly and the natural convection from the exposed surfaces. Having reached the steady state for each heat loss test, the heating power is balanced with the heat loss which is recorded along with the corresponding averaged wall-to-ambient temperature difference in order to correlate the equation capable of evaluating the heat loss flux. The detailed q distributions over the scanned surface are obtained by subtracting the local heat loss flux from the regional heat fluxes.

The dimensionless pressure drop over the entire two-pass rib-roughened test channel is calculated as the Fanning friction factors (f) based on the pressure drops (ΔP) across the entire test channel of length L with the mean flow velocity (W_m) and pressure (ρ) evaluated from the inlet of test channel as $f = [\Delta P/(0.5\rho W_m^2)]/(d/4T_L)$. The thermal performance factor (η) at each tested Re with and without bleed is accordingly determined as $\eta = (\overline{Nu}/Nu_\infty)/(f/f_\infty)^{1/3}$ based on constant pumping power consumptions.

The final phase of program analyzes the f coefficients for the entire test channel as well as the spatially averaged heat transfer data ($\overline{Nu}_I$, $\overline{Nu}_O$, $\overline{Nu}_T$) and the η factors over the inlet, outlet-legs and the turning region of the present two-pass rib-roughened channel. Comparisons of the f coefficient, regionally averaged Nu and the η factor are performed for the non-bleed and three bleed conditions. A set of empirical correlations for $\overline{Nu}_I$, $\overline{Nu}_O$, and $\overline{Nu}_T$, and f coefficients is derived with no-bleed and three bleed conditions using Re and BR as the determining variables.

The maximum uncertainties of Nu, f, and Re are estimated following the policy of ASME on reporting the uncertainties in experimental measurements and results (ASME JHT Editorial Board, 1993). For this class of heat-transfer experiments, the temperature measurements are the major sources for the uncertainties in Nu, f, and Re as the properties of the test coolant such as thermal conductivity and viscosity are evaluated in accordance with the local fluid bulk temperature. Based on the repeatability calibration tests for the present infrared thermal image system, the maximum uncertainty of the wall temperature measurement is estimated as ± 0.7 °C. The maximum uncertainties of the derived parameters for constituting the governing dimensionless groups are estimated as: heat flux (0.9%), fluid viscosity (0.38%), fluid thermal conductivity (0.3%), and fluid specific heat (0.1%). The maximum uncertainties associated with Nu, Re, and f were respectively estimated as 9.8%, 5.4% and 2.9%.

3. Results and discussion

3.1. Re and BR impacts on Nusselt numbers

The detailed Nu distributions over the rib floor of the two-pass test channel with the bleed from the location referred to as the inlet-leg, middle-turn, or the outlet-leg at Re = 25,000 are collected in

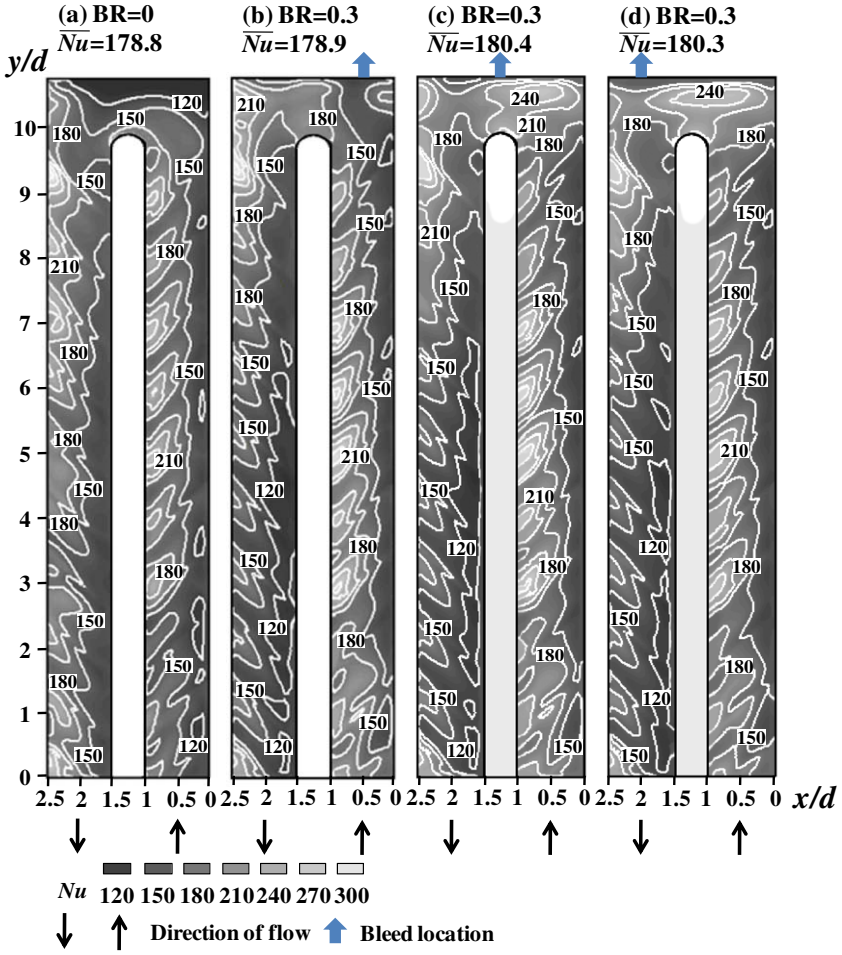

Fig. 3. Detailed Nu distributions over rib-roughened floor for three bleed conditions with BR = 0, 0.1, 0.2, and 0.3 at Re = 25,000.

Fig. 3 to typify the impacts of bleed from the outer wall of the sharp bend on the heat transfer performance. The plots depicted in Fig. 3 compares the *Nu* distributions obtained at BR = 0.3 with the bleed from a designated location on the outer wall of the sharp bend. Cross comparisons of the *Nu* plots in Fig. 3 reveal the impacts of the location of bleed on *Nu* distributions. Within the flow region upstream the sharp bend about one channel hydraulic diameter (d) in the inlet-leg, the levels and patterns of *Nu* distributions showed by all the *Nu* plots in Fig. 3 are almost identical. Within the flow region downstream the sharp bend about one d in the outlet-leg, the distributing patterns of *Nu* showed by all the plots in Fig. 3 are in close agreements. But, after reviewing all the *Nu* results obtained with BR = 0.1, 0.2, and 0.3, the *Nu* levels are consistently reduced as BR increases from 0.1 to 0.3. In the inlet-leg upstream and the outlet-leg downstream the sharp bend about one d, the similar distributing *Nu* patterns for all the BR examined are indicative of the similar flow sutures developed within. While the reduced *Nu* levels in the outlet-leg driven by increasing the coolant extractions from the referred outlet-leg location are caused by the reduced airflow rate downstream the bleed, which in turn reduces the actual Reynolds number (Re^*) in the outlet-leg. With BR = 0, 0.1, 0.2, and 0.3Re^* are respectively equal to 1, 0.9, 0.8, and 0.7*Re* in the outlet-leg. The impact of 180° turn on the heat transfer performances in the inlet-leg is initiated at about 1d upstream the sharp bend and ended at about 1d downstream the sharp bend in the outlet-leg. In the flow regions where the effects of sharp bend on the shape of *Nu* contours are diminished, the *Nu* plots depicted in Fig. 3 over the inlet and outlet-legs recast the typical heat transfer results in a straight rib-roughened channel in which the streamwise *Nu* peaks develop on the rib-tops and at the mid-rib locations close to the reattachment points. In addition, the *Nu* levels consistently decay from the obtuse edge of the rib floor, where the skewed ribs incline at 135° from the main flow direction, toward the acute edge in both inlet and outlet-legs due to the vortical flows tripped by these angled ribs. In the inlet-leg, the repetitive *Nu* variations develop after the airflow traverses four pairs of ribs; while the pattern of periodical *Nu* variations in the outlet-leg resumes quickly at its second rib after the sharp bend. As compared in Fig. 3, the distinct differences in *Nu* distributions between the inlet-leg and the turning region and between the outlet-leg and the turning section are clearly visible due to the different flow structures developed in these flow regions.

In the turning region with no bleed, a low *Nu* stripe initiates from the outer corner of the inlet-leg where the re-circulating flow develops (Viswanathan and Tafti, 2006) and proceeds along the outer edge of the sharp bend. With the present rib arrangement and the smooth turning section, the bulk airflow through the sharp bend is directed to impinge toward the outer corner and its downstream outlet-leg sidewall where coincide with the regions of high *Nu*. Downstream of the bend, a small region of low *Nu* attaches on the inner wall of the divider where the small recirculation zone is developed (Viswanathan and Tafti, 2006). When the airflow turns its direction from the inlet-leg into the sharp bend, it accelerates locally and separates at the top circular edge of the central divider along which a rim of high *Nu* is emerging. With a bleed from the outer wall of the sharp bend, the *Nu* distributions over the turning section as compared in Fig. 3 are considerably modified from the no-bleed condition and are characterized by the location of the bleed. Examinations of all the *Nu* plots collected at BR = 0.1, 0.2, and 0.3 indicate that the distributing patterns of *Nu* over the turning section are not modified by different BR but varied with the location of the bleed.

The bleed from the outer wall of the sharp bend breaks the boundary layers surrounding the bleed hole, modify the vortical flow structures in the sharp bend and add the favorable pressure gradients to improve the fluency of the turning flow that distorts and weakens the re-circulating corner flows in the likewise no-bleed channel. These bleed-induced favorable mechanisms for HTE effects elevate the regional *Nu* over the turning section from the no-bleed levels. However, the reduction of airflow downstream the bleed decreases *Re* and increases T_b which effects together reduce *Nu* and increase T_w in the outlet-leg. The trade-offs between the elevated and reduced *Nu* over the respective turning section and outlet-leg have caused the $\overline{Nu}$ over the entire rib floor of the two-pass bleed channel to be slightly higher than the no-bleed counterparts. But the variations of the regional *Nu* over the turning section and the outlet-leg ($\overline{Nu}_T$ and $\overline{Nu}_0$) from the no-bleed references are substantial, which will be later examined in more details. It is also clearly visible in Fig. 3 for all three bleed conditions that the low *Nu* stripe along the outer wall of the sharp bend in the no-bleed channel has diminished considerably; while the rim of high *Nu* attached on the top circular edge of the central divider expands toward the outer wall of the sharp bend. In the two-pass rib-roughened channel with no bleed, the numerically detected Dean-vortices at the center of the 180° bend, which impinge on the inner and outer walls in the bend, were reported as the dominant flow features to induce high *Nu* at these walls (Viswanathan and Tafti, 2006). With a bleed located at the outer wall of the sharp bend, the developments of Dean-vortices through the turning section are modified by the bleed. Unlike the *Nu* distributions over the turning section in the no-bleed channel, the bleed has induced a high *Nu* region between the outer and the inner circular walls of the sharp bend. As compared by Fig. 3, the location of the single bleed on the outer wall of the sharp bend has a profound influence on the location and the range of such high *Nu* region emerging between the outer and the inner circular walls over the central turning section. With the bleed from the middle-turn or from the outlet-leg location as depicted in Fig. 3c and d, the high *Nu* regions on the central turning section emerge at locations toward the inlet-leg sidewall; while such high *Nu* regions are shifted toward the outlet-leg sidewall when the bleed is extracted from the inlet-leg. After examining all the heat transfer results obtained at BR = 0.1, 0.2, and 0.3, the degree of HTE impact over the high *Nu* regions along the outlet-leg sidewall and on the central turning section is systematically weakened as BR increases for the referred inlet-leg bleed condition. In this respect, the BR impacts on heat transfer performances over the turning region are mainly caused by the reduced mass flux of the airflow downstream each bleed in the sharp bend. As a result, it is expected the heat transfer performance over the turning section of the present two-pass ribbed channel is interdependent with *Re*, BR and the location of the bleed.

To examine the influences of *Re* and the bleed location on heat transfer enhancement over the turning section, Fig. 4 compares the distributions of Nu/Nu_∞ over the turning section detected from *Re* = 5000, 15,000, and 25,000 for BR = 0 and 0.3 with the bleed from (a) inlet-leg, (b) middle-turn, and (c) outlet-leg. The impacts of *Re* and the bleed location on Nu/Nu_∞ distributions over the turning section for the bleed conditions of (a) inlet-leg, (b) middle-turn, and (c) outlet-leg are respectively revealed by comparing the Nu/Nu_∞ plots collected in each row and each column of Fig. 4. With no bleed, the pattern of Nu/Nu_∞ distributions over the turning section remains unchanged for all the *Re* tested. The review of all the heat transfer results generated from all the test *Re* and BR indicates that the regionally averaged Nu/Nu_∞ over the turning section of the bleed channel ($\overline{Nu}_T/Nu_\infty$) with all three bleed conditions are elevated from the no-bleed references but decrease with the increase of BR from 0.1 to 0.3. It is worth noting that $\overline{Nu}_T/Nu_\infty$ at each tested bleed condition decreases as *Re* increases. This result reflects that the power index of *Re* in $\overline{Nu}_T$ correlation is less than the 0.8*Re* index in Nu_∞ correlation. By treating $\overline{Nu}_T/Nu_\infty$ as the heat transfer enhancement ratio, the HTE impact for the present ribbed channel

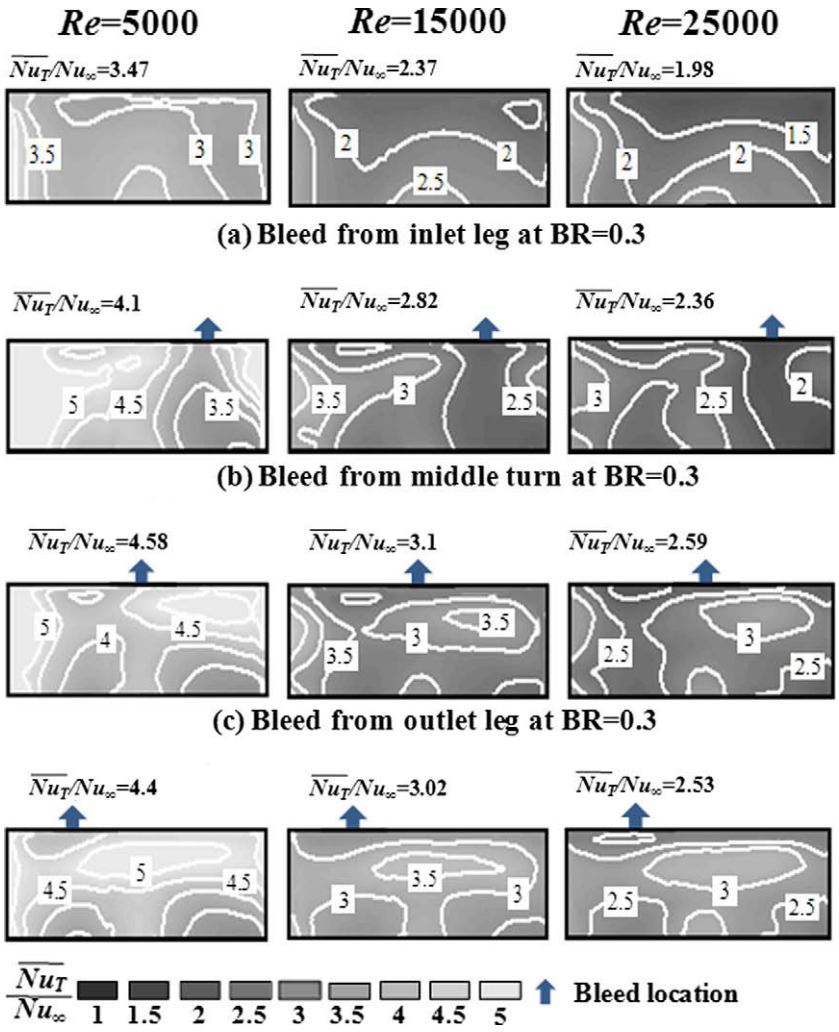

Fig. 4. Detailed distributions of Nu/Nu_∞ over turning section of test channel with BR = 0, 0.1, 0.2, and 0.3 at Re = 5000, 10,000, 15,000, 20,000, and 25,000.

with and without bleed decreases as Re increases. With the bleed from the outer wall of the sharp bend at the projected center of the inlet-leg sectional plane which is referred to as the inlet-leg bleed as seen in Fig. 4a, a high Nu/Nu_∞ spike emerges from the high heat transfer region along the outlet-leg sidewall toward the location of the bleed. In the inlet-leg bleed channel, the development of such Nu/Nu_∞ spike indicates that the impingement of turning flow still promotes HTE effects on the outlet-leg sidewall of the sharp bend but the vortical structures within the turning bulk stream are modified by the bleed in the manner to stimulate the high convective performances downstream the middle section of the sharp bend. The extent and levels of such high Nu/Nu_∞ spike as shown in each plot of Fig. 4a systematically decreases as Re increases; or increases as BR decreases from 0.3 to 0.1 after examining all the Nu/Nu_∞ plots generated by this study. Relative to the no-bleed Nu/Nu_∞ conditions at each Re tested as seen by comparing the plots collected in each row of Fig. 4a, the structure of re-circulating cell at the corner of sharp bend on the inlet-leg sidewall is disrupted by the inlet-leg bleed so that the low heat transfer region around this corner in the no-bleed channel is diminished. Due to the high Nu/Nu_∞ spike emanating from the outlet-leg sidewall of the sharp bend, the Nu/Nu_∞ levels over the downstream half of the turning section are generally higher than the upstream counterparts for the inlet-leg bleed channel as shown in Fig. 4a. When the coolant is extracted from the middle-turn on the outer wall of the sharp bend, an additional high Nu/Nu_∞ region is also observed in Fig. 4b between the outer and inner walls of the sharp bend but the location of such high Nu/Nu_∞ region is shifted toward the inlet-leg sidewall from the scenario found in the channel with the inlet-leg bleed. The extent and levels of the high Nu/Nu_∞ region between the inner and outer walls of the sharp bend in the middle-turn bleed channel also decrease as Re increases or as BR decreases. The impingement of the turning bulk stream through the sharp bend still elevates local Nu/Nu_∞ over the outlet-leg sidewall. The bleed-induced high Nu/Nu_∞ region between the outer and inner walls of the sharp bend tends to be merged with the high Nu/Nu_∞ region on the outlet-leg sidewall when Re is increased or BR is decreased. In this respect, it is clearly seen in Fig. 4b with Re = 25,000 that a high Nu/Nu_∞ stripe develops across the entire span-width of the sharp bend between the outer and inner walls of the sharp bend. But the Nu/Nu_∞ distributions shown in Fig. 4b are not symmetric about the central plane of the sharp bend even if the bleed is located at the middle-turn on the outer wall of the sharp bend due to the asymmetrical pressure fields in the sharp bend. The cross examination of the Nu/Nu_∞ plots collected in Fig. 4a–c indicates that the heat transfer enhancement at the no-bleed inlet-leg corner of the sharp turn are much improved for the channels with middle-turn or outlet-leg bleed relative to the conditions observed with the inlet-leg bleed channel. With the bleed from the outlet-leg location, the Nu/Nu_∞ plots over the

turning section as shown in Fig. 4c share great similarities with those depicted by Fig. 4b; but the high Nu/Nu_∞ region developed between the inner and outer walls of the sharp bend as seen in Fig. 4c is shifted toward the outlet-leg sidewall when the location of bleed on the outer wall of the sharp bend is changed from the middle-turn to the outlet-leg location. Clearly, the *Re* and BR impacts on the distributions of Nu/Nu_∞ over the sharp bend for each bleed channel as demonstrated by Fig. 4 have caused $\overline{Nu}_T$ to be interdependent with *Re* and BR.

The overall heat transfer performances over the inlet-leg, turning section and outlet-leg are assessed by comparing the averaged Nusselt numbers ($\overline{Nu}_I$, $\overline{Nu}_T$, $\overline{Nu}_O$) over these regional areas on the scanned rib floor at each *Re* and BR tested. This is demonstrated by Fig. 5 in which the variations of $\overline{Nu}_I$, $\overline{Nu}_T$, and $\overline{Nu}_O$ against *Re* at BR = 0, 0.1, 0.2, and 0.3 are compared. Fig. 5a, d and g also compare the present normalized Nusselt numbers in terms of $\overline{Nu}_I/Nu_\infty$ with the data reported by different research groups [15,16] for validations. As seen in Fig. 5a, d and g, three *Re* controlled $\overline{Nu}_I$ curves at all BR tested converge into a tight data band at each *Re* tested, indicating the vanished BR effect on $\overline{Nu}_I$. As the regionally averaged heat transfer performance over the inlet-leg is not affected by the bleed from the turning section, the present $\overline{Nu}_I/Nu_\infty$ data compare favorably with the heat transfer data detected from the likewise no-bleed channels [15,16]. The $\overline{Nu}_I/Nu_\infty$ showed in Fig. 5a, d, and g fall systematically from 3.6 to 2.5 as *Re* increases from 5000 to 25,000. In the turning section as compared in Fig. 5b, e and h, the coolant extraction from the outer wall of the sharp turn at each bleed location causes the attendant $\overline{Nu}_T$ elevations from the no-bleed counterparts with the higher degrees of $\overline{Nu}_T$ augmentations at the middle-turn and the outlet-leg bleed conditions. Such bleed-driven $\overline{Nu}_T$ elevations from the no-bleed datum increase as *Re* increases due to the development of *Re*-driven high *Nu* stripe between the inner and outer walls of the sharp bend as demonstrated by Fig. 4. In this respect, there are about 25–35% of $\overline{Nu}_T$ increments from the no-bleed references over the turning section due to the single bleed from the outer wall of the sharp bend. Although the extent of BR impacts on $\overline{Nu}_T$ for each bleed channel as seen in Fig. 5b, e or h remains less than 10%, the increase of BR from 0.1 to 0.3 causes the consistent reductions in $\overline{Nu}_T$ for each bleed condition. But the cross examination of the *Nu* references over the inlet-leg and the turning section for the no-bleed channel as compared in Fig. 5 indicates that $\overline{Nu}_T$ are reduced about 20% from $\overline{Nu}_I$ due to the re-circulating flow cells developed in the sharp turn of the no-bleed channel. These interesting heat transfer results indicate that each bleed condition at BR = 0.1 can sufficiently yield the flow structures in the sharp bend that lead to the $\overline{Nu}_T$ elevations from the no-bleed references. Such flow modifications in the sharp bend at BR = 0.1 are likely to be remained at BR = 0.2 and 0.3 but the further reductions of downstream airflows from each bleed location weaken the convective performances over the turning region. As the mass flux of coolant downstream the bleed is reduced, the area-averaged Nusselt numbers over the outlet-leg of each bleed channel ($\overline{Nu}_O$) are reduced from the no-bleed references. In this regard, the increase of BR form 0.1 to 0.3 has incurred the systematic $\overline{Nu}_O$ reductions to the extent about 25% from the no-bleed $\overline{Nu}_O$ datum. As demonstrated previously in Fig. 3, the influences of bleed on *Nu* distributions prevails only about one channel hydraulic diameter upstream and downstream of the sharp bend in the inlet and outlet-legs respectively. The impact of bleed location from the outer wall of the sharp bend on $\overline{Nu}_I$ and $\overline{Nu}_O$ is negligible. But the $\overline{Nu}_O$ reductions in the outlet-leg of the present two-pass channels due to the bleed from the sharp bend as seen in Figs. 5c, f and i are undesirable in blade cooling applications, which are attributed to the decreases in *Re*. It is worth noting that, the decrease in airflow rates downstream the bleed can reduce $\overline{Nu}_O$ by reducing *Re* and elevate the wall temperatures over the outlet-leg due to the decreased $\overline{Nu}_O$ and the reducing airflow rate downstream the bleed. The attendant T_b increase due to the reduced downstream airflow rate from the bleed location has profound influences on T_w elevations, which effect can not be overlooked at the design stage. However, as the actual Reynolds numbers in the outlet-leg of the bleed channels are Re^*, the variations of

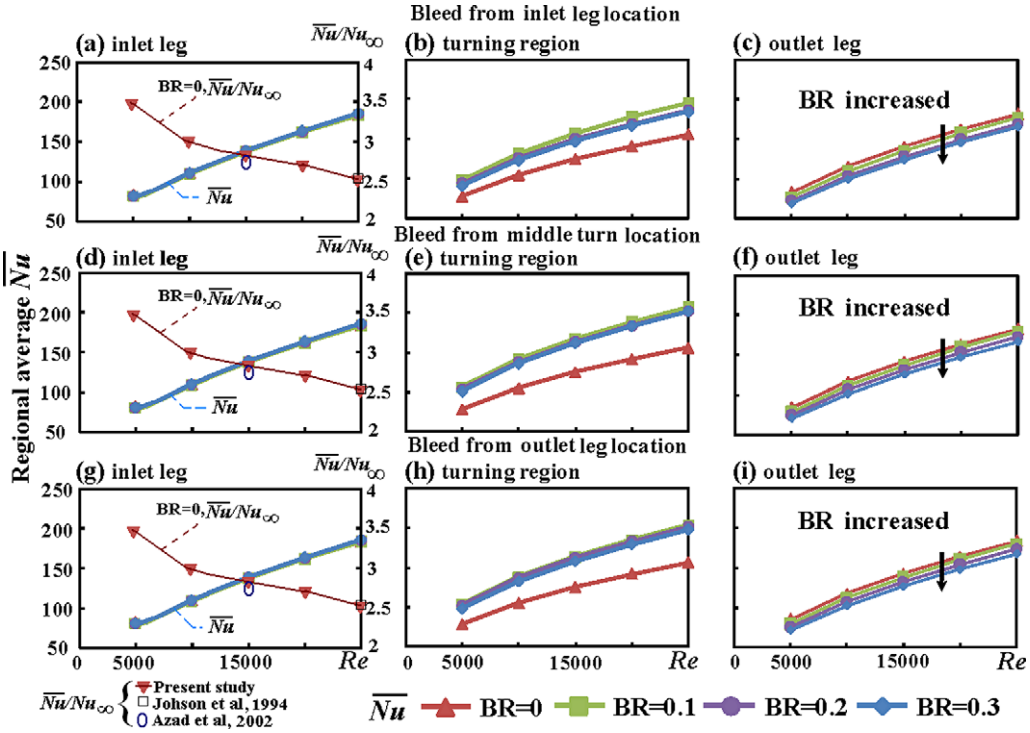

Fig. 5. Variations of $\overline{Nu}_{I,T,O}$ against *Re* at BR = 0, 0.1, 0.2, and 0.3.

$\overline{Nu}_O$ against Re^* with BR = 0, 0.1, 0.2, and 0.3, which are representative for three bleed conditions, are converged into a tight data trend controlled by Re^* as seen in Fig. 6. Unlike the systematic downward $\overline{Nu}_O$ spreads driven by increasing BR as shown in Fig. 5c, f and i, each $\overline{Nu}_O$ versus Re^* trend collected from BR = 0, 0.1, 0.2 or 0.3 as seen in Fig. 6 are assembled as a segment of the single Re^* controlled $\overline{Nu}_O$ curve. The Re^* controlled $\overline{Nu}_O/Nu_\infty$ curve also agrees favorably with the comparable data collected from the inlet-leg of the multi-pass ribbed channels (Johnson et al., 1994; Azad et al., 2002). Therefore the overall heat transfer performances for the present outlet-leg with and without bleed from the sharp bend are dominated by the typical flow mechanisms developed in a straight square duct with two opposite walls roughened by 45° ribs. The various BR impacts on $\overline{Nu}_O$ depicted in Fig. 5c, f and i can be well correlated by a single Re^* controlled function.

Based on the heat transfer results collected in Fig. 4 and 5 which show that $\overline{Nu}_I$, $\overline{Nu}_T$, and $\overline{Nu}_O$ consistently increase as Re increases, a general data trend with the limiting condition of diminished forced convective capability ($\overline{Nu} \to 0$) as $Re \to 0$ is followed by all the results. The correlations for $\overline{Nu}_I$, $\overline{Nu}_T$, and $\overline{Nu}_O$ are accordingly derived as Eq. (1) in which the coefficient $A_{I,T,O}$ and exponent $B_{I,T,O}$ are functions of BR and the location of the bleed for $\overline{Nu}_T$.

$$\overline{Nu}_{I,T,O} = A_{I,T,O}\{BR\} \times Re^{B}_{I,T,O}\{BR\} \quad (1)$$

Table 2 summarizes the $\overline{Nu}_I$, $\overline{Nu}_T$, and $\overline{Nu}_O$ correlations derived for the present test channels. Justified by the results depicted in Fig. 6, it is interesting to find that the $\overline{Nu}_T$ correlation yields into the identical format of $\overline{Nu}_I$ by replacing Re with Re^*.

The experimental measurements of $\overline{Nu}_I$, $\overline{Nu}_T$, and $\overline{Nu}_O$ are compared with the correlative results calculated by Eq. (1) to examine the overall success of these heat transfer correlations. As compared in Fig. 7, 98% of the present experimental data is found to agree

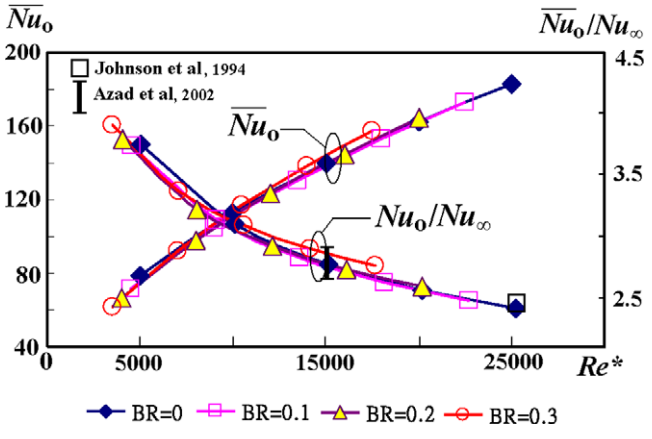

Fig. 6. Variations of $\overline{Nu}_O$ against Re^* at BR = 0, 0.1, 0.2, and 0.3.

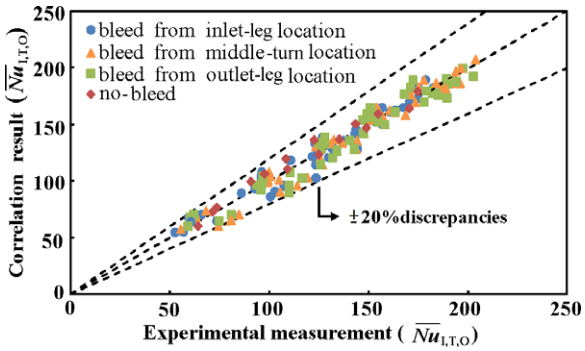

Fig. 7. Comparison of experimental and correlative $\overline{Nu}_{I,T,O}$ at all bleed conditions.

within +20% of the correlations proposed over the entire range of the parametric conditions examined. In general, the clustered heat transfer data obtained with the middle-turn and the outlet-leg bleed conditions show the higher Nusselt numbers than the counterparts with inlet-leg bleed. This is mainly caused by the higher $\overline{Nu}_T$ for the channels with the middle-turn and the outlet-leg bleed conditions; while the data clusters collected from the bleed channels can also fall below than the no-bleed datum because $\overline{Nu}_O$ are generally reduced from the no-bleed references due to the decreased airflow rates in the outlet-leg of the two-pass channel. While recognizing that the bleed from the sharp bend generates the aforementioned heat transfer impacts on local and area-averaged Nu, the engine designer has to be noted that the reference fluid temperature selected for Nu definition is the local T_b which increases at a higher streamwise gradient downstream the bleed. The attendant T_w variations in the downstream direction after the bleed therefore increase with the higher streamwise gradients even if the Nusselt numbers over the inlet and outlet-legs were identical. The wall temperatures deduced from the variation in Nusselt number reported by this study needs to consider the bleed effect on local T_b.

3.2. Re and BR impacts on pressure drops and thermal performance factors

The bleed from the outer wall of the sharp bend not only improves the thermal performances in the sharp bend as demonstrated in previous section, but also reduces the pressure drops through the present two-pass channel. This is demonstrated by comparing the variations of the pressure drop coefficients (f) against Re at three bleed locations with BR = 0, 0.1, 0.2, and 0.3 in Fig. 8. The f values collected in Fig. 8 are evaluated from the pressure drops across the entire length of the present two-pass channel with the characteristic flow velocity selected as the mean flow velocity at the entrance of the inlet-leg for both bleed and no-bleed

Table 2
$\overline{Nu}_I$, $\overline{Nu}_T$, $\overline{Nu}_O$ correlations.

$\overline{Nu}_{I,T,O} = A_{I,T,O}BR \times Re^{B_{I,T,O}BR}$		
$\overline{Nu}_I$	$0.876 \times Re^{0.53}$	
$\overline{Nu}_T$		
Bleed location	Coefficient A	Exponent B
Inlet-leg	$1.55 + 11.13 \times BR - 59.5 \times BR^2 + 81.66 \times BR^3$	$0.452 - 0.115 \times BR + 0.15 \times BR^2 + 1.01 \times BR^3$
Middle-turn	$1.55 + 17.53 \times BR - 87 \times BR^2 + 116.6 \times BR^3$	$0.452 - 0.301 \times BR + 1.05 \times BR^2 - 0.333 \times BR^3$
Outlet-leg	$1.55 + 13.91 \times BR - 67.5 \times BR^2 + 83.33 \times BR^3$	$0.452 - 0.211 \times BR + 0.7 \times BR^2 + 0.166 \times BR^3$
$\overline{Nu}_O$		
	$0.876 \times \{(1 - BR) \times Re\}^{0.53}$	

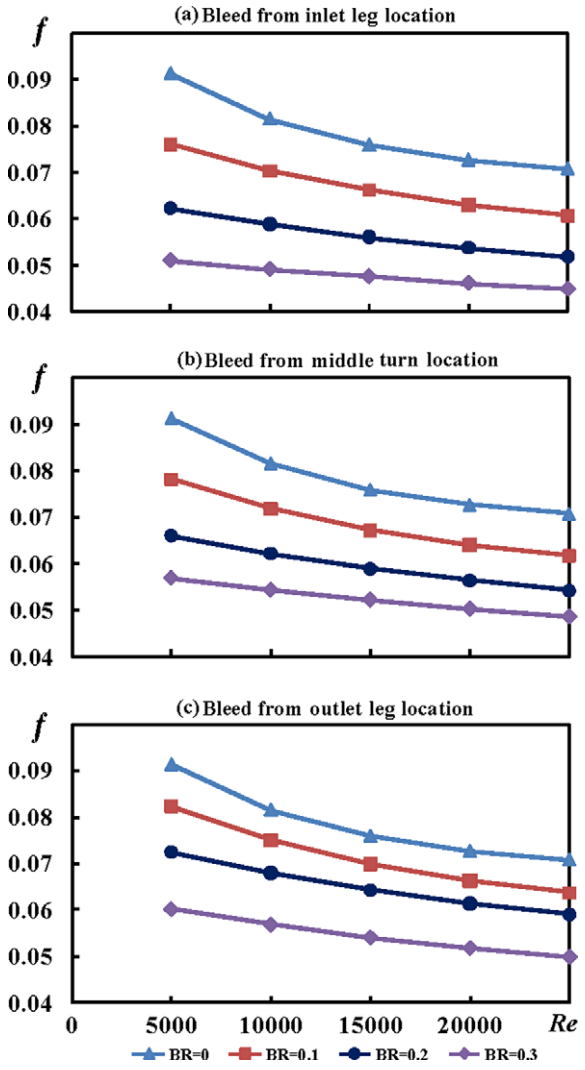

Fig. 8. Variations of f against Re with bleed conditions of (a) inlet-leg, (b) middle-turn, and (c) outlet-leg at BR = 0, 0.1, 0.2, and 0.3.

channels. For each test channel with BR = 0, 0.1, 0.2, and 0.3 as shown in Fig. 8, the pressure drop coefficients (f) follow the exponential decay as Re increases. As compared in each plot of Fig. 8, the no-bleed channel (BR = 0) consistently operates at the higher f values than those in the bleed channels to large extents. The adverse pressure gradients in the sharp bend of the no-bleed channel, which trigger several local flow separations and lead to the development of re-circulating flow cells within, are considerably diminished in each bleed channel. A bleed from the outer wall of the sharp bend increases $\overline{Nu}_T$ with f reductions from the no-bleed conditions. Nevertheless, such bleed reduces $\overline{Nu}_O$ and increases T_b gradient downstream the bleed. As BR increases from 0.1 to 0.3, the f values for each bleed condition are accordingly reduced. About 30–40% of f reductions are observed in Fig. 8 for each bleed channel at BR = 0.3. In this respect, the inlet-leg bleed condition offers the higher degrees of f reductions from the conditions resolved in the middle-turn and outlet-leg bleed channels. Justified by the data trends depicted in Fig. 8, the f correlation expressed as the function of Re for each bleed channel shares a general form of Eq. (2).

$$f_{I,T,O} = L_{I,T,O}\{BR\} + M_{I,T,O}\{BR\} \times e^{-}N\{BR\} \times Re \quad (2)$$

Coefficients L, M, N in Eq. (2) for each bleed condition examined here are functions of BR. The plots of $L_{I,T,O}$, $M_{I,T,O}$, $N_{I,T,O}$ against BR also vary in the exponential form with the asymptotic limit at BR = 0 to recover the results detected from the no-bleed channel. Table 3 summarizes the $L_{I,T,O}$, $M_{I,T,O}$, $N_{I,T,O}$ equations expressed as functions of BR.

The calculated f factors using Eq. (1) are compared with the experimental measurements to assess the accuracies of these f correlations. As compared in Fig. 9, all the experimental f data converge within +20% of the correlations proposed. While all the f data detected from the bleed channels as compared in Fig. 8 are less than the no-bleed levels at each Re examined, the clustered f data obtained with the inlet-leg bleed condition as shown in Fig. 9 depict the lowest values from the counterparts collected from both middle-turn and outlet-leg bleed channels.

As an overall assessments for each bleed channel based on constant pumping power consumptions, the thermal performance factor (η) are defined as $(\overline{Nu}/Nu_\infty)/(f/f_\infty)^{1/3}$ in which $\overline{Nu}$ is the averaged Nusselt number over the entire two-pass rib floor and f is evaluated from the pressure drop across the entire test channel. Using the Nu results collected in Fig. 3 as an illustrative example, it has been previously illustrated that the respective bleed-driven Nu elevations and impediments over the turning section and the outlet-leg have neutralized the bleed impacts on $\overline{Nu}$. But the bleed impacts on the regional thermal performances as demonstrated in Fig. 5 still remain evident. Nevertheless, the considerable reductions in pressure drops through each bleed channel from the no-bleed conditions can still elevate the η factors in each bleed channel as compared in Fig. 10 for BR = 0.1, 0.2, and 0.3. As seen in Fig. 10, the η factors detected from each bleed channel are constantly higher than the no-bleed counterparts in the present Re range but consistently decrease as Re increases for bleed and no-bleed channels. As a typical heat transfer characteristic for

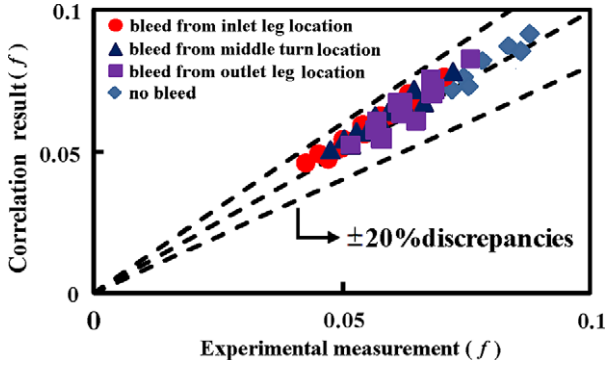

Fig. 9. Comparison of experimental and correlative f factors at all bleed conditions.

Table 3
$L_{I,T,O}$, $M_{I,T,O}$, $N_{I,T,O}$ coefficients.

Bleed location	$f_{I,T,O} = L_{I,T,O}\{BR\} + M_{I,T,O}\{BR\} \times e^{-N\{BR\}\times Re}$		
	L function	M fuction	N function
Inlet-leg	$0.018 + 0.0503 \times e^{-3.47\times BR}$	$-0.00243 + 0.0423 \times e^{-2.55\times BR}$	$1.68E{-}5 + 9.31E{-}5 \times e^{-7.58\times BR}$
Middle-turn	$0.0119 + 0.0565 \times e^{-0.026\times BR}$	$0.0143 + 0.0256 \times e^{-4.05\times BR}$	$8.96E{-}6 + 1.01E{-}4 \times e^{-5.62\times BR}$
Outlet-leg	$-0.0165 + 0.0856 \times e^{-1.27\times BR}$	$-1.39 + 1.43 \times e^{-0.04\times BR}$	$2.78E{-}5 + 8.26E{-}5 \times e^{-7.22\times BR}$

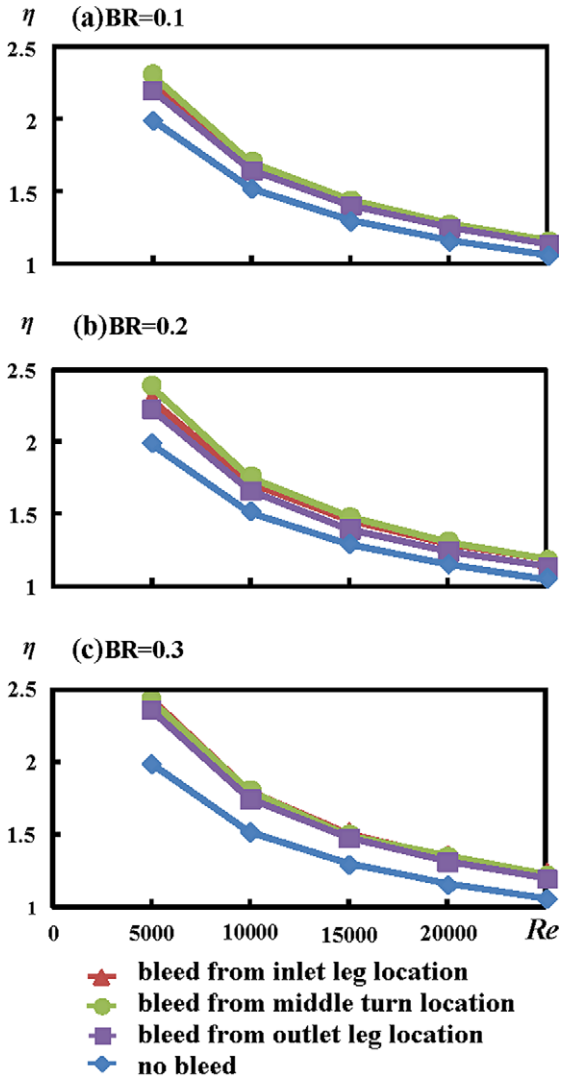

Fig. 10. Variations of η against Re at BR = (a) 0.1, (b) 0.2, and (c) 0.3 for all bleed conditions.

rib-roughened channels, the B exponents in $\overline{Nu}_{I,T,O}$ correlations indicated in Table 2 are all less than 0.8 in the Nu_∞ correlation so that the $\overline{Nu}/Nu_\infty$ ratio consistently decreases as Re increases. This Re-driven reduced HTE effect in terms of $\overline{Nu}/Nu_\infty$ ratio for each test channel at BR = 0, 0.1, 0.2, and 0.3 has led to the consistent declination in η factor as Re increases as shown in each plot of Fig. 10. As compared in each plot of Fig. 10, the location of bleed from the outer wall of the sharp bend provide negligible impacts on η factors at each BR tested so that the three η factors acquired from different bleed conditions at each Re converge into a tight data band. The cross comparison of η levels between Fig. 10a–c for each bleed condition tested reveals that the η factors consistently increase as BR increases from 0.1 to 0.3 due to the substantial reductions in f factors as BR increases. Referring to Fig. 5, $\overline{Nu}_O$ decreases as BR increases from 0.1 to 0.3. Although the reductions in f are achievable by increasing BR for the present two-pass bleed channel, the undesirable $\overline{Nu}_O$ impacts triggered by increasing BR can not be overlooked during the design stage.

4. Conclusions

The following salient remarks emerge from the experimental results generated by this investigation.

1. Nu distributions over the inlet and outlet-legs with and without bleed recast the typical results in a likewise straight ribbed channel. Without bleed, a low Nu stripe along the outer edge of the sharp bend emerges over the turning section. With a bleed, a high Nu stripe emerges between the outer and inner walls of the sharp bend. The location and spatial range of such high Nu stripe over the turning region vary with the bleed location but is insensible to BR.
2. While the value of $\overline{Nu}_I$ is in agreement with those in likewise no-bleed channels, the reduction of airflow downstream the bleed from the sharp bend considerably reduces $\overline{Nu}_O$ to the extents of about 25% of the no-bleed references at BR = 0.3. Such BR impacts on $\overline{Nu}_O$ are well correlated by Re^*. With a bleed from the sharp bend, $\overline{Nu}_T$ are considerably elevated from the no-bleed references but decreased as BR increases. The bleed-driven $\overline{Nu}_T$ elevation increases as Re increases.
3. As BR increases from 0.1 to 0.3, f factors are accordingly reduced for each bleed channel with about 30–40% of f reductions at BR = 0.3. The inlet-leg bleed condition provides the higher degree of f reduction than that with a bleed from the middle-turn or outlet-leg.
4. Thermal performance factors (η) detected from each bleed channel are consistently higher than the no-bleed references but decreases as Re increases because $\overline{Nu}/Nu_\infty$ for each test channel decrease as Re increases. While η increases consistently as BR increases from 0.1 to 0.3 due to the substantial f reductions as BR increases, the location of bleed from sharp bend provides negligible impacts on η.
5. The experimental correlations for $\overline{Nu}_{I,T,O}$ and $f_{I,T,O}$ with Re and BR as the determining variables are respectively derived as Eqs. (1) and (2) for the present two-pass rib-roughened square channel with bleed from the outer wall of the sharp bend.

Acknowledgement

This work was funded by the National Science Council, Taiwan, R.O.C. under the Grant number, NSC 94-2611-E-022-001. Additional assistances provided by my research student Bo-Jun Huang are appreciated.

References

Azad, G.S., Uddin, M.J., Han, J.C., Moon, K.-H., Glezer, B., 2002. Heat transfer in a two-pass rectangular rotating channel with 45-deg angled rib turbulators. J. Turbomach. 124, 251–259.
Chang, S.W., Yang, T.L., Huang, R.F., Sung, K.C., 2007. Influence of channel height on heat transfer in rectangular channels with skewed ribs at different bleed conditions. Int. J. Heat Mass Transfer 50, 4581–4599.
Chang, S.W., Liou, T.-M., Chiou, S.F., Chang, S.F., 2008. Heat transfer in high-speed rotating trapezoidal duct with rib-roughened surfaces and air bleeds from the wall on apical side. ASME J. Heat transfer 130, 061702-1–061702-13.
Chanteloup, D., Bölics, A., 2002. Flow characteristics in two-leg internal coolant passages of gas turbine airfoils with film-cooling hole ejection. ASME J. Turbomach. 124, 499–507.
Chanteloup, D., Wolfersdorf, J.V., 2004. Analysis of a transient heat transfer experiment in a two pass internal coolant passage. Int. J. Heat Mass Transfer 47, 5313–5322.
Dittus, F.W., Boelter, L.M.K., 1930. Publications in Engineering, vol. 2. University of California, Berkeley, CA. p. 443.7.
Editorial Board of ASME Journal of Heat Transfer, 1993. Journal of heat transfer policy on reporting uncertainties in experimental measurements and results. ASME J. Heat Transfer 115, 5–6.
Ekkad, S.V., Han, J.-C., 1997. Detailed heat transfer distributions in two-pass square channels with rib turbulators. Int. J. Heat Mass Transfer 40, 2525–2537.
Ekkad, S.V., Hung, Y., Han, J.C., 1998. Detailed heat transfer distributions in two-pass square channels with rib turbulators and bleed holes. Int. J. Heat Mass Transfer 41, 3781–3791.
Ekkad, S.V., Pamula, G., Shantiniketanam, 2000. Detailed heat transfer measurements inside straight and tapered two-pass channels with rib turbulators. Exp. Therm. Fluid Sci. 22, 155–163.
Grag, V.K., 2002. Heat transfer research on gas turbine airfoils at NASA GRC. Int. J. Heat Fluid Flow 23, 109–136.

Iacovides, H., Jackson, D.C., Kelmenis, G., Launder, B.E., Yuan, Y.-M., 2001. Flow and heat transfer in a rotating U-bend with 45° ribs. Int. J. Heat Fluid Flow 22, 308–314.

Iacovides, H., Launder, B.E., 2007. Internal blade cooling: the Cinderella of computational and experimental fluid dynamics research in gas turbines, 2007. In: Proceedings of the Institution of Mechanical Engineers, Part A. J. Power Energy 221, 265–290.

Johnson, B.V., Wagner, J.H., Steuber, G.D., Yeh, F.C., 1994. Heat transfer in rotating serpentine passages with trip skewed to the flow. ASME J. Turbomach. 116, 113–123.

Parsons, J.A., Han, J.C., Zhang, Y., 1995. Effect of model and wall heating condition on local heat transfer in a rotating two-pass square channel with rib turbulators. Int. J. Heat Mass Transfer 38, 1151–1159.

Shen, J.R., Wang, Z., Ireland, P., Jones, T.V., Byerley, A.R., 1996. Heat transfer enhancement with a turbine blade cooling passage using ribs and combinations of ribs with film cooling holes. ASME J. Turbomach. 118, 428–434.

Taslim, M.E., Li, T., Spring, S.D., 1995. Experimental study of the effects of bleed holes on heat transfer and pressure drop in trapezoidal passages with tapered turbulators. ASME J. Turbomach. 117, 281–289.

Thurman, D., Poinsatte, P., 2001. Experimental heat transfer and bulk air temperature measurements for a multipass internal cooling model with ribs and bleed. ASME J. Turbomach. 123, 90–96.

Viswanathan, A.K., Tafti, D.K., 2006. Detached eddy simulation of turbulent flow and heat transfer in a two-pass internal cooling duct. Int. J. Heat Mass Transfer 27, 1–20.